Interaction potential and infrared absorption of endohedral H2 in C60

Min Ge, U. Nagel, D. Hüvonen, T. Rõõm, S. Mamone et al.

Additional information on J. Chem. Phys.

Interaction potential and infrared absorption of endohedral H₂ in C₆₀

Min Ge,[1] U. Nagel,[1] D. Hüvonen,[1] T. Rõõm,[1,a)] S. Mamone,[2] M. H. Levitt,[2] M. Carravetta,[2] Y. Murata,[3] K. Komatsu,[3] J. Y.-C. Chen,[4] and N. J. Turro[4]

[1]*National Institute of Chemical Physics and Biophysics, Akadeemia tee 23, 12618 Tallinn, Estonia*
[2]*School of Chemistry, Southampton University, Southampton SO17 1BJ, United Kingdom*
[3]*Institute for Chemical Research, Kyoto University, Kyoto 611-0011, Japan*
[4]*Department of Chemistry, Columbia University, New York, New York 10027, USA*

We have measured the temperature dependence of the infrared spectra of a hydrogen molecule trapped inside a C₆₀ cage, H₂@C₆₀, in the temperature range from 6 to 300 K and analyzed the excitation spectrum by using a five-dimensional model of a vibrating rotor in a spherical potential. The electric dipole moment is induced by the translational motion of endohedral H₂ and gives rise to an infrared absorption process where one translational quantum is created or annihilated, $\Delta N = \pm 1$. Some fundamental transitions, $\Delta N = 0$, are observed as well. The rotation of endohedral H₂ is unhindered but coupled to the translational motion. The isotropic and translation–rotation coupling part of the potential are anharmonic and different in the ground and excited vibrational states of H₂. The vibrational frequency and the rotational constant of endohedral H₂ are smaller than those of H₂ in the gas phase. The assignment of lines to *ortho-* and *para-*H₂ is confirmed by measuring spectra of a *para* enriched sample of H₂@C₆₀ and is consistent with the earlier interpretation of the low temperature infrared spectra [Mamone *et al.*, J. Chem. Phys. **130**, 081103 (2009)]. © *2011 American Institute of Physics.* [doi:10.1063/1.3535598]

I. INTRODUCTION

The advancement of "molecular surgery" has led to the breakthrough in experimental studies of hydrogen molecules trapped inside fullerene cages. This method[1–3] results in sample quantities of the order of 100 mg and has made possible nuclear magnetic resonance (NMR),[4,5] infrared (IR),[6] and inelastic neutron scattering (INS) (Refs. 7 and 8) spectroscopic investigations of the trapped H₂ dynamics and stimulated theoretical investigations.[9–12] It has been established that H₂ inside a C₆₀ cage is an unhindered vibrating rotor performing translational motion in a nearly spherical potential well.[13] Similar properties have been predicted theoretically for CO@C₆₀ with an additional strong mixing of translational and rotational motions due to the heteronuclear nature of the endohedral molecule.[14] Another known endohedral diatomic rotor, C₂@Sc₂C₈₄, is two-dimensional and shows hindered rotation.[15,16]

The H₂@C₆₀ represents a system where the simplest molecule is encapsulated by a molecule with the highest symmetry. The vibrational, rotational, and translational levels of H₂ inside the cage are well separated because of the small mass of the hydrogen atom. The high icosahedral symmetry of the C₆₀ cavity is close to spherical. The local environment of H₂ has a negligible inhomogeneous distribution of parameters, and there is one H₂ per trapping site. The H₂@C₆₀ is a stable complex and can survive a short period of heating up to 500°C under vacuum.[3] These properties make H₂@C₆₀ appealing for spectroscopic and theoretical investi-

gations of interactions between the molecular hydrogen and curved nanosurfaces.

The complications that make the system interesting stem from the hydrogen molecule. *First*, because H₂ is not spherical, its interaction potential with C₆₀ depends on the orientation of its molecular axis relative to the inner surface of the C₆₀ cage,[17] an interaction called translation–rotation coupling. If the translational and the rotational motions are coupled, then in the spherical potential the conserved angular momentum is the sum of translational and rotational angular momenta.[9,18] The translation–rotation coupling is measured as a splitting of absorption lines in the IR spectrum.[6] *Second*, vibrational and translational motion amplitudes of H₂ are relatively large because of its small mass. This makes the potential for H₂ translational motion anharmonic and dependent on the vibrational state. *Third*, the symmetry relative to the interchange of two protons dictates that there are two forms of molecular hydrogen, called *para-* and *ortho-*H₂. The two proton spins ($I_p = 1/2$) are in the antisymmetric $I = 0$ total nuclear spin state in *para-*H₂ and in the symmetric $I = 1$ state in *ortho-*H₂. Even rotational quantum numbers J are allowed for *para-*H₂ and odd J for *ortho-*H₂. As a consequence the *ortho-*H₂ ground state is above the *para-*H₂ ground state by about 120 cm⁻¹, the energy difference between $J = 0$ and 1 rotational energy levels. At room temperature, the equilibrium distribution of H₂ spin isomers is $n_o/n_p = 3$. The time constant of thermal relaxation between the *ortho* and the *para* manifolds is very long. The relaxation process can be speeded up by using a spin catalyst. For H₂@C₆₀ it is feasible to reach the thermal equilibrium at liquid nitrogen temperature (77 K), $n_o/n_p = 1$, using liquid oxygen as a spin catalyst for *ortho–para* conversion.[19,20]

a)Electronic mail: toomas.room@kbfi.ee.

The IR spectrum of H_2@C_{60} at 6 K, presented and analyzed in Ref. 6, consists of sharp lines positioned between 4000 and 5000 cm^{-1}. The initial and final states for the transitions are the vibrational ground state $v = 0$ and the excited state $v = 1$. The IR activity of H_2 is induced by the translational motion of H_2 relative to the C_{60} cage, giving rise to a selection rule $\Delta N = \pm 1$, where N is the translational quantum number. However, the transitions between *para* and *ortho* states are still forbidden, and from this a selection rule, $\Delta J = 0, \pm 2$ follows. The allowed transitions are shown with solid lines in Fig. 1. At low T only the $v = 0$, $N = 0$ state is populated and only transitions to the $N = 1$ translational state in the excited vibrational state are allowed by the selection rule $\Delta N = \pm 1$, shown with black solid lines in Fig. 1. The fundamental $\Delta v = 1$, $\Delta N = 0$ *para* and *ortho* absorption lines were detected too (dashed lines in Fig. 1), although 2 orders of magnitude weaker than $\Delta N = 1$ lines. This additional information, the frequencies of the fundamental lines, allowed the determination of the energy separation of $N = 0$ and $N = 1$ translational levels in the $v = 1$ state.

Based on the available data it has not been possible to separate the harmonic and the anharmonic parts of the bounding potential, experienced by H_2. The information about the potential in the ground $v = 0$ state is limited, too. The separation of $N = 0$ and $N = 1$ translational levels is known from the INS experiment.[8] The translation–rotation splitting of the
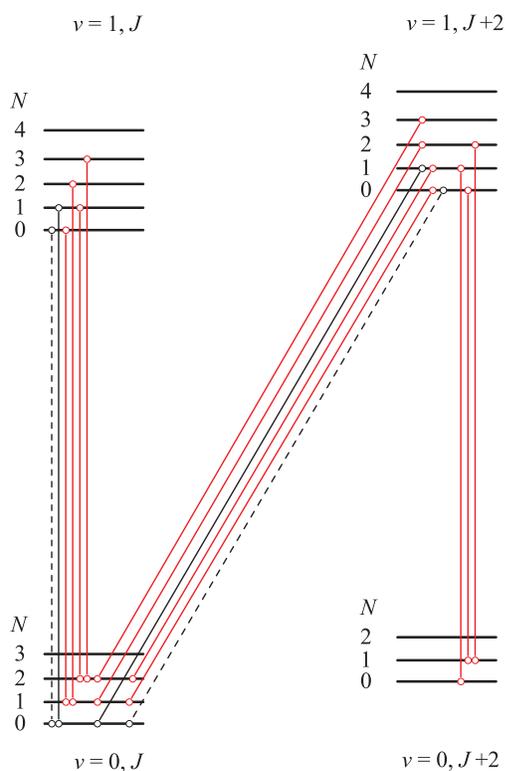
$N = 1$ translational state of *ortho*-H_2@C_{60} has not been resolved in the ground vibrational state, likely because of the limited spectral resolution of INS.

In this paper we present and analyze the temperature dependence of IR spectra between 6 and 300 K. At elevated temperatures, levels up to $N = 2$ in the $v = 0$ state are sufficiently populated to give rise to detectable IR transitions to terminal states connected to the initial states by the selection rules $\Delta v = 1$, $\Delta N = \pm 1$, and $\Delta J = 0, 2$. From this spectral information, we have determined the potential, including translation–rotation coupling and anharmonic corrections, for both vibrational states $v = 0$ and $v = 1$. We have confirmed the assignment of spectral lines to *ortho*- and *para*-H_2 using an *ortho–para* converted sample.

II. THEORY

The theoretical work of Olthof *et al.*[14] is a comprehensive description of the dynamics of a loosely bound *molecule* inside C_{60}. They calculated the dynamics and the IR spectra of CO@C_{60}. The main differences between their approach and ours are the following. First, Olthof *et al.* model the intermolecular potential as a sum of atom–atom potentials and expand it in spherical harmonics. We expand the confining potential in spherical harmonics as well but determine the expansion parameters by fitting the calculated IR spectra to our experimental data. The second difference is in the calculation of IR line intensities. The CO molecule has a permanent dipole moment, while in H_2@C_{60} the dipole moment is induced by the translational motion of H_2.

A. Five-dimensional spherically symmetric Hamiltonian of H₂@C₆₀

To describe the motion of H_2 inside C_{60} we use the following model. The C_{60} is considered to be rigid, its center of mass is not moving, and it does not rotate. We treat H_2@C_{60} as an isolated molecular complex and approximate the true icosahedral symmetry of an isolated C_{60} with spherical symmetry. It means that in this approximation H_2 moves in a rigid spherically symmetric bounding potential provided by the cavity of C_{60}. Besides the translational movement inside C_{60}, the H_2 molecule has its internal degrees of freedom, vibration and rotation of two protons relative to its center of mass. There are no coupling terms between *ortho*-H_2 (J odd) and *para*-H_2 (J even) states in our model Hamiltonian. Compared to our earlier work[6] the model has been extended in few points. Here we include the centrifugal correction term D_e to the rotational constant B_e and add an anharmonic term $^v V_{00}^{224}$ to the anisotropic confining potential. The basis has been extended to $N \leq 7$ for *both* vibrational states, $v = 0$ and $v = 1$. A more detailed description of the model follows.

The position and orientation of the H_2 molecule are given by spherical coordinates $\mathbf{R} = \{R, \Omega\}$, $\Omega = \{\Theta, \Phi\}$ and $\mathbf{s} = \{s, \Omega_s\}$, $\Omega_s = \{\theta, \phi\}$, where $\mathbf{R}$ is the vector from the center of the C_{60} cage to the center of mass of H_2 and $\mathbf{s}$ is the internuclear H–H vector, as shown in Fig. 2.

FIG. 1. Diagram of the observed IR transitions. The diagram describes *para*-H_2 states if the rotational quantum number $J = 0$ and *ortho*-H_2 states if $J = 1$. Vibrational quantum number is v and translational quantum number is N. The additional structure of energy levels $E^v_{JNL\Lambda}$ due to quantum numbers L and Λ is not shown. Dashed lines are forbidden transitions, and black lines are the only transitions that are observable at low temperature (see also Fig. 2 in Ref. 6).
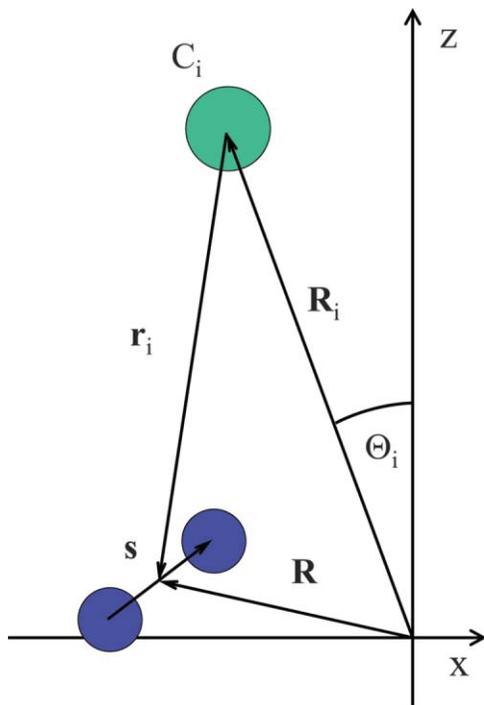
FIG. 2. Coordinates to describe the H$_2$ dynamics and the induced dipole moment inside the C$_{60}$ cage. C$_i$ is the ith carbon atom with coordinates $\mathbf{R}_i$ relative to the C$_{60}$ cage center. $\mathbf{r}_i$ shows the position of the H$_2$ center of mass relative to ith carbon atom. $\mathbf{s}$ gives the relative position of two protons and $\mathbf{R}$ is the H$_2$ center of mass displacement from the C$_{60}$ cage center.

To describe the center of mass translational motion of H$_2$, we use eigenfunctions of the isotropic three-dimensional harmonic oscillator:[21]

$$\Psi^v_{NLM_L}(R, \Omega) = \psi^v_{NL}(R)\, Y_{LM_L}(\Omega), \qquad (1)$$

where ψ^v_{NL} is the radial wavefunction and Y_{LM_L} is the spherical harmonic. The size of the H$_2$ molecule depends on its vibrational state. Therefore, both the bounding potential and $\psi^v_{NL}(R)$ depend on the vibrational quantum number v. The translational quantum numbers are $N = 0, 1, 2, \ldots$. The orbital angular momentum quantum number takes values $L = N, N - 2, \ldots, 1$ or 0, depending on the parity of N, and the azimuthal quantum number is $M_L = -L, -L + 1, \ldots, L$. The rotational wavefunctions, defined by the rotational quantum numbers $J = 0, 1, \ldots$ and $M_J = -J, -J + 1, \ldots, +J$, are given by the spherical harmonics $Y_{JM_J}(\theta, \phi)$.

We use bipolar spherical harmonics with an overall spherical rank Λ and a component M_Λ, defined as

$$F^{LJ}_{\Lambda M_\Lambda}(\Omega, \Omega_s) = \sum_{M_L, M_J} \mathcal{C}^{\Lambda M_\Lambda}_{LM_L J M_J} Y_{LM_L}(\Omega) Y_{JM_J}(\Omega_s), \qquad (2)$$

where $\mathcal{C}$ is the Clebsch–Gordan coefficient.[22] Then the full wavefunction describing the motion of the H$_2$ molecule is

$$|v J N L \Lambda M_\Lambda\rangle = \psi^{\text{vib}}_v(s)\psi^v_{NL}(R)F^{LJ}_{\Lambda M_\Lambda}(\Omega, \Omega_s), \qquad (3)$$

where $\psi^{\text{vib}}_v(s)$ is the vibrational wavefunction with the quantum number v.

The Hamiltonian $\mathcal{H}$ for the trapped molecule includes coupling terms between vibrational, translational, and rotational motions. For simplicity, we neglect all matrix elements nondiagonal in v and introduce a parametric dependence on v:

$$\mathcal{H} = {}^v\mathcal{H}^{\text{vib-rot}} + \frac{p^2}{2m} + {}^v V(R, \Omega, \Omega_s), \qquad (4)$$

where ${}^v\mathcal{H}^{\text{vib-rot}}$ is the vibration–rotation Hamiltonian, p is the molecular momentum operator, and m is the molecular mass of H$_2$. Here, ${}^v V$ is the potential energy of the H$_2$ molecule in the vibrational state $\psi^{\text{vib}}_v(s)$. The vibration–rotation Hamiltonian ${}^v\mathcal{H}^{\text{vib-rot}}$ is diagonal in the basis set $|v J N L \Lambda M_\Lambda\rangle$, with eigenvalues given by

$$^v E^{\text{vib-rot}}_J = \hbar\omega_0(v + 1/2) + B_r J(J + 1), \qquad (5)$$

where $B_r = B_e - \alpha_e(v + 1/2) - D_e J(J + 1)$, ω_0 is the fundamental vibration frequency, α_e is the anharmonic correction, and D_e is the centrifugal correction to the rotational constant B_e.[23,24]

The potential energy expanded in multipoles is

$$^v V(R, \Omega, \Omega_s) = \sum_{n,l,j,\lambda,m_\lambda} {}^v V^{ljn}_{\lambda m_\lambda} R^n F^{lj}_{\lambda m_\lambda}(\Omega, \Omega_s), \qquad (6)$$

where the functions F are defined in Eq. (2) and n takes even values. Translation–rotation coupling terms are terms with nonzero l, j. All odd-j terms vanish for homonuclear diatomic molecules. For an icosahedral cavity, and assuming that longer-range intermolecular perturbations are negligible, all terms with odd λ values vanish, as well as the terms with $\lambda = 2$ and 4. We assume that all high-order terms starting from $\lambda = 6$ are small and express the potential energy as $^v V = {}^v V^0 + {}^v V'$. The isotropic harmonic term is given by $^v V^0 = {}^v V^{002}_{00} R^2 F^{00}_{00}$, where we have neglected the constant offset $^v V^{000}_{00} F^{00}_{00}$. The perturbation $^v V'$ consists of translation–rotation coupling $^v V^{222}_{00}$ and anharmonic corrections $^v V^{004}_{00}$ and $^v V^{224}_{00}$ to both isotropic and anisotropic couplings,

$$^v V' = \left({}^v V^{222}_{00} R^2 + {}^v V^{224}_{00} R^4\right) F^{22}_{00} + {}^v V^{004}_{00} R^4 F^{00}_{00}. \qquad (7)$$

The unperturbed Hamiltonian eigenvalues in the basis $|v J N L \Lambda M_\Lambda\rangle$ are given by

$$E^0_{v J N L \Lambda M_\Lambda} = {}^v E^{\text{vib-rot}}_J + \hbar\, {}^v\omega^T_0 (N + 3/2), \qquad (8)$$

where $^v\omega^T_0$ is the frequency for translational oscillations within the cavity,

$$^v\omega^T_0 = \left({}^v V^{002}_{00}/(2\pi m)\right)^{1/2}. \qquad (9)$$

B. Induced dipole moment and line intensities

Here we are interested in the dipole moment of the hydrogen–fullerene complex induced by the motion of the hydrogen molecule inside the fullerene cage. We derive the dependence of the induced dipole moment on translational coordinates $\mathbf{R} = \{R, \Omega\}$ and rotational coordinates $\Omega_s = \{\theta, \phi\}$ of H$_2$ and relate the dipole moment to the IR absorption line area. The explicit dependence on R is particularly useful as, *first*, the radial part of the translational wavefunction $\psi^v_{NL}(R)$ is different in vibrational states $v = 0$ and

$v = 1$, which are the initial and final states of IR transitions. *Second*, the initial state is not only the $N = 0$ state as was the case when the low T spectra were analyzed,[6] but other states with $N > 0$ are thermally populated, too. To derive the induced dipole moment for $H_2@C_{60}$, we assume that it is the sum of dipole moments induced by pairwise interactions between H_2 and ith carbon atom.

An overview of collision induced dipoles in gases and gas mixtures is given in the book by Frommhold.[25] The confinement of the endohedral H_2 introduces two differences as compared to H_2 in the gas. *First*, the translational energy of H_2 is quantized. In the gas phase it is a continuum starting from zero energy. *Second*, the variation of the distance between H_2 and the carbon atom is limited to the translational amplitude of H_2 in the confining potential. In the gas phase the distance varies from infinity to the minimal distance given by the collision radius. The selection rule $\Delta N = \pm 1$ for the endohedral H_2 follows from these two conditions, as shown below. Quantum mechanical calculations of induced dipoles are available for simple binary systems like H_2–He, H_2–Ar, and H_2–H_2. An extensive set of theoretical results for the H_2–He system associated with the roto-translational electric dipole transitions, both in the vibrational ground state $v = 0$ and accompanying the $v = 0 \rightarrow 1$ transition of the H_2 molecule, can be found in Refs. 26–30.

The dipole moment operator for H_2 and ith carbon atom can be expanded in spherical harmonics[31]

$$d_q(\mathbf{r}_i, \mathbf{s}) = \frac{4\pi}{\sqrt{3}} \sum_{l,j=0}^{\infty} B^{lj}(r_i, s) F_{1q}^{lj}(\Omega_i, \Omega_s), \qquad (10)$$

where $q = 0, \pm 1$ denotes the spherical component of the dipole moment vector $\mathbf{d}$ and the spherical functions $F_{1q}^{lj}(\Omega_i, \Omega_s)$ are described by Eq. (2). The position of the ith carbon atom is defined by $\mathbf{R}_i = \{R_i, \Omega_{Ci}\}$, $\Omega_{Ci} = \{\Theta_i, \Phi_i\}$, and the position of the center of mass of H_2 relative to the ith carbon atom by vector $\mathbf{r}_i = \{r_i, \Omega_i\}$, $\Omega_i = \{\theta_i, \phi_i\}$, as shown in Fig. 2. The origin of coordinates of $\mathbf{R}_i$ and $\mathbf{R}$ is chosen in the geometric center of C_{60}. We introduce the dependence of dipole moment on the initial and the final vibrational states, $d_{q,v'v}(\mathbf{r}_i, \Omega_s) \equiv \langle \psi_{v'}^{\mathrm{vib}}(s) | d_q(\mathbf{r}_i, \mathbf{s}) | \psi_v^{\mathrm{vib}}(s) \rangle$. Using Eq. (10) and the vibrational part of wavefunctions (3) we get that the dependence of dipole moment on the proton–proton distance s is absorbed by the B term: $B_{v'v}^{lj}(r_i) \equiv \langle \psi_{v'}^{\mathrm{vib}}(s) | B^{lj}(r_i, s) | \psi_v^{\mathrm{vib}}(s) \rangle$.

Since the dipole moment is a vector, there are restrictions on the allowed j and l values of the H_2–C pair: (i) $j + l$ must be odd, (ii) $l = j \pm 1$ from the triangle relation, and (iii) for homonuclear molecules only even j terms are allowed. We discuss here the first three terms, B^{10}, B^{12}, and B^{32}. B^{10} corresponds to the induced dipole moment which is independent of the orientation of H_2 molecular axis. B^{12} describes the exchange interaction induced dipole which depends on the H_2 molecular axis orientation. B^{32} is the term describing the dipole moment induced on the "collision" partner by the quadrupolar moment of H_2 and is called the quadrupolar induction term. In the spherical approximation and in the first order of displacement of H_2 from the C_{60} cage center, the quadrupolar induction term is zero (see below).

We expand the dipole moment $d_{q,v'v}(\mathbf{r}_i, \Omega_s)$ between the ith C atom and H_2 into a Taylor series in powers of $\mathbf{R}$ at the center of C_{60} and sum over all carbon atoms. The zero order term vanishes because $\mathbf{R} = 0$ is the center of inversion for $H_2@C_{60}$. We keep the first nonzero term which is linear in $\mathbf{R}$:

$$d_{q,v'v}^{(1)}(\mathbf{R}, \Omega_s) = \frac{4\pi}{\sqrt{3}} \sum_{i,l,j} \mathbf{R} \cdot \nabla_{\mathbf{r}_i} \left[B_{v'v}^{lj}(r_i) F_{1q}^{lj}(\Omega_i, \Omega_s) \right]_{\mathbf{r}_i = -\mathbf{R}_i}, \qquad (11)$$

where $\nabla_{\mathbf{r}_i}$ is the nabla operator in the spherical coordinates of $\mathbf{r}_i$. Instead of summation over carbon atoms, we integrate and assume that the distance from the cage center is the same for all carbon atoms, $R_i \simeq R_0$. One can relate the result of integration to the expansion of the dipole moment in terms of spherical harmonics of angular coordinates (Ω, Ω_s):

$$d_{q,v'v}^{(1)}(\mathbf{R}, \Omega_s) = \frac{4\pi}{\sqrt{3}} \sum_{l,j} A_{v'v}^{lj}(R) F_{1q}^{lj}(\Omega, \Omega_s). \qquad (12)$$

The nonzero coefficients are $A_{v'v}^{10}$ and $A_{v'v}^{12}$ where

$$A_{v'v}^{lj}(R) = 20 \, R \, B_{v'v}[lj], \qquad (13)$$

and we have used the notation

$$B_{v'v}[lj] = \left. \frac{\partial B_{v'v}^{lj}(r)}{\partial r} \right|_{r=R_0} + \frac{2}{R_0} B_{v'v}^{lj}(R_0). \qquad (14)$$

The calculation shows that in the spherical approximation of C_{60} and in the first order of $\mathbf{R}$ the quadrupolar induction term $A_{v'v}^{32}$ vanishes to zero. The selection rules for IR spectroscopy of $H_2@C_{60}$ follow from the angular and radial dependence of $d_{q,v'v}^{(1)}$ [Eq. (12)]: $\Delta N = \pm 1$ and change of the total angular momentum is $\Delta \Lambda = 0, \pm 1$ with $\Delta J = 0, \pm 2$ and $\Delta L = \pm 1$.

The absorption line area (unit m^{-2}) in the limit that the linewidth is much smaller than the transition frequency ω_{if} is

$$S(\omega_{if}) = \frac{\mathcal{N} \pi}{V \eta c \epsilon_0 \hbar} p_i \omega_{if} \left| \langle f | \hat{\mathbf{e}} \cdot \mathbf{d} | i \rangle \right|^2, \qquad (15)$$

where $\hat{\mathbf{e}} = \mathbf{E}/E$ is the unit vector of light electric field $\mathbf{E}$, $\mathcal{N}/V = 1.48 \times 10^{27}$ m^{-3} is number density of molecules in solid C_{60}, c is the speed of light ϵ_0 is the permittivity of vacuum, η is the index of refraction (in C_{60} $\eta = 2$, Ref. 32), $\hbar$ is the reduced Planck constant, $\omega_{if} = (E_f - E_i)/(2\pi \hbar c)$ is the number of waves in one meter, where E_i (E_f) is the energy of the initial state $|i\rangle$ (the final state $|f\rangle$), p_i is the probability that the initial state is populated, and $\mathbf{d}$ is the dipole moment (unit Cm).

The module of the matrix element for depolarized light and randomly oriented molecules is

$$\langle | \langle f | \hat{\mathbf{e}} \cdot \mathbf{d} | i \rangle |^2 \rangle = \frac{1}{3} \sum_{\zeta = x', y', z'} |\langle f | d_\zeta | i \rangle|^2, \qquad (16)$$

where d_ζ are the components of the dipole moment in the molecular frame $\{x', y', z'\}$. In the case of spherical symmetry all three terms in Eq. (16) are equal and we may write using the $q = 0$ component of the dipole moment (12),

$$S(\omega_{if}) = \frac{\mathcal{N} \pi}{V \eta c \epsilon_0 \hbar} p_i \, \omega_{if} \left| \langle f | d_{0,v'v}^{(1)}(\mathbf{R}) | i \rangle \right|^2. \qquad (17)$$

C. Fitting of IR spectra

First the experimental IR absorption spectrum was fitted using Gaussian lineshapes to find the line areas, linewidths, and frequencies. A synthetic experimental spectrum $y(\omega_n)$, the distance between the points in the spectrum $\omega_n - \omega_{n-1} = \Delta\omega/4$, was then generated consisting of lines with equal linewidths, $\Delta\omega = 1$ cm^{-1}, while keeping the line areas and frequencies of the original experimental lines. The synthetic spectrum approach was needed as our model did not include any line broadening mechanism. For a given model and basis, matrix elements of the Hamiltonian and the dipole operator were evaluated analytically in a symbolic form. At each step of minimizing $\chi^2 = \sum[y - f(\omega_n, \{\kappa\})]^2$, the numerical values were substituted for symbols and the Hamiltonian diagonalized numerically. Here $f(\omega_n, \{\kappa\})$ is the theoretical spectrum with linewidths and lineshape identical to the synthetic experimental spectrum; $\{\kappa\}$ is the set of fit parameters: the *ortho–para* ratio, Hamiltonian and dipole operator parameters. As first partial derivatives are zero at the best fit, we used second derivatives to calculate the error margins $\Delta\kappa_i$ of the fit parameters,

$$\Delta\kappa_i = \sqrt{\chi^2 \left(\frac{\partial^2 \chi^2}{\partial \kappa_i^2}\right)^{-1}}. \tag{18}$$

After the initial determination of reasonable starting values $\{\kappa\}$, we assigned the main absorption lines to *ortho* and *para* groups and further refined the starting values for proceeding with this nonlinear fit. Before the final rounds of the fit, we assigned the main absorption lines to transitions between certain eigenstates and verified this by their temperature dependence.

In the spherical approximation the energy does not depend on M_Λ. Therefore, it is practical to use a reduced basis and reduced matrix elements[33] which are independent of M_Λ. This reduces the number of states by a factor of $2\Lambda + 1$ for each Λ. The values of other quantum numbers we used to define the eigenstates $|vJNL\Lambda\rangle$ were $v = 0$ and 1, $J \leq 3$, and $N \leq 7$. In such reduced basis there are 192 *para*-H$_2$ and 292 *ortho*-H$_2$ states.

In the line intensity calculation (17) the sum includes all possible M_Λ allowed by the initial and final state Λ. This sum can be reduced to the form of reduced dipole matrix elements, $\langle\tau_f\Lambda_f||d^{(1)}||\tau_i\Lambda_i\rangle$, of the dipole operator (12) using the relation,[33]

$$\sum_{M_{\Lambda_f}, M_{\Lambda_i}} \left|\langle\tau_f\Lambda_f M_{\Lambda_f}\left|d_q^{(1)}\right|\tau_i\Lambda_i M_{\Lambda_i}\rangle\right|^2$$
$$= \frac{1}{3}|\langle\tau_f\Lambda_f||d^{(1)}||\tau_i\Lambda_i\rangle|^2, \tag{19}$$

where $|\tau\rangle \equiv |vJNL\rangle$. To calculate the IR absorption line area, the formula,

$$S(\omega_{if}) = \frac{\mathcal{N}\pi 10^{-2}}{3V\eta c\epsilon_0\hbar} p_i \omega_{if} |\langle\tau_f\Lambda_f||d^{(1)}||\tau_i\Lambda_i\rangle|^2, \tag{20}$$

was used, where all units are SI, except ω in cm^{-1} and the absorption line area S in cm^{-2} units.

If the thermal relaxation between *para*-H$_2$ and *ortho*-H$_2$ is very slow we can define a temperature independent fractional *ortho* and *para* populations n_k of the total number of molecules $\mathcal{N}$, where $k = o, p$ selects *ortho*- or *para*-H$_2$. Then the probability that the initial state is populated is

$$p_i = n_k \frac{(2\Lambda_i + 1)e^{-E_i/k_BT}}{\sum_j(2\Lambda_j + 1)e^{-E_j/k_BT}}, \tag{21}$$

where E_i is the energy of the initial state measured from the ground state $v = N = 0$ and j runs over all *para*- (or *ortho*-) H$_2$ states in the basis used.

III. EXPERIMENT

H$_2$@C$_{60}$ was prepared at Kyoto University by molecular surgery method as described in Ref. 3. The *para* enriched sample was made at Columbia University using molecular oxygen as a spin catalyst for *ortho–para* conversion.[19] Briefly, the H$_2$@C$_{60}$ adsorbed on the external surface of NaY zeolite was immersed in liquid oxygen at 77 K for 30 min, thereby converting the incarcerated H$_2$ spin isomers to the equilibrium distribution at 77 K, $n_o/n_p = 1$. The liquid oxygen was pumped away and the endofullerene–NaY complex was brought back rapidly to room temperature. The *para* enriched H$_2$@C$_{60}$ was extracted from the zeolite with CS$_2$, and the solvent was evaporated by argon. The powder sample in argon atmosphere and on dry ice arrived in Tallinn 4 days after the preparation.

The pellets of H$_2$@C$_{60}$ for IR transmission measurements were pressed under vacuum. The diameter of sample pellets was 3 mm and thickness $d = 0.25$ mm (H$_2$@C$_{60}$) or $d = 0.12$ mm (*para* enriched H$_2$@C$_{60}$). Two identical vacuum tight chambers with Mylar windows were employed in the IR measurements. The chambers were put inside an optical cold finger type cryostat with KBr windows. In the measurements, the chamber containing the pellet for analysis was filled with He exchange gas, while the empty chamber served as a reference. Transmission spectra were obtained using a Bruker interferometer Vertex 80v with a halogen lamp and a HgCdTe or an InSb detector. The apodized resolution was typically 0.3 cm^{-1} or better.

Transmission $T_r(\omega)$ was measured as the light intensity transmitted by the sample divided by the light intensity transmitted by the reference. Figure 3 shows the transmission spectra of H$_2$@C$_{60}$ at 6 and 300 K between 3800 and 4900 cm^{-1}. The absorption coefficient $\alpha(\omega)$ was calculated from the transmission $T_r(\omega)$ through $\alpha(\omega) = -d^{-1}\ln[T_r(\omega)(1 - R)^{-2}]$, with the reflection coefficient $R = [(\eta - 1)/(\eta + 1)]^2$ calculated assuming a frequency independent index of refraction,[32] $\eta = 2$. Absorbance spectra were cut into shorter pieces around groups of H$_2$ lines and a baseline correction was performed before fitting the H$_2$ lines with Gaussians.

IV. RESULTS

Transmission spectra of H$_2$@C$_{60}$ at 6 and 300 K between 3800 and 4900 cm^{-1} are shown in Fig. 3. Sharp lines close to 3850, 4250, 4600, and 4800 cm^{-1} are from IR absorption of trapped H$_2$. The main difference between 6 and 300 K spectra
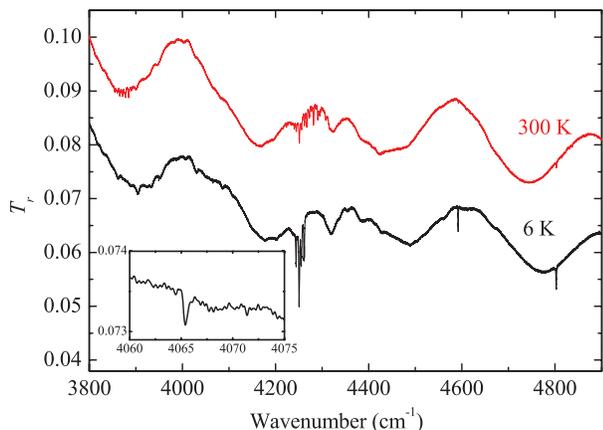
FIG. 3. Transmission spectra of H_2@C_{60} at 6 K (lower curve, black) and 300 K (upper curve, red) between 3800 and 4900 cm^{-1}. The inset shows much weaker fundamental $\Delta N = \Delta J = 0$ *ortho* (4065.4 cm^{-1}) and *para* (4071.4 cm^{-1}) lines at 6 K. The broad interference fringes with 300 cm^{-1} spacing are caused by the difference in the optical thickness of the sample and reference cell windows.

FIG. 5. Spectra in the region around 4250 cm^{-1} of a *para* enriched H_2@C_{60} (solid line) measured at 20 K (a) and 300 K (b) compared to spectra of the same sample after 19 days at 300 K, dashed line in (b), and nonenriched sample at 6 K (a).

is an additional group of lines in the 300 K spectrum at about 3850 cm^{-1}.

We compared the C_{60} absorption lines in the region from 2400 to 3500 cm^{-1}, calculated from the transmission of the single crystal spectrum[34] and from our powder sample transmission spectrum. The C_{60} absorption lines in the single crystal and powder sample spectrum had similar intensities when the background was subtracted, and we concluded that although the overall transmission level in our polycrystalline sample is lower than that in the single crystal spectrum, the line intensities are not affected by the light scattering.

The temperature dependence of the IR absorption spectrum of H_2@C_{60} is shown in Fig. 4. The spectral lines involving transitions from the $N = 0$ state are present at 6 K. At 90 K, more lines are visible and they correspond to the transitions starting from the $N = 1$ state. At 200 K, additional lines are present where the initial state is $N = 2$. Broad lines that are visible already in the 6 K spectrum below 4000 cm^{-1} in Fig. 4(a) are not H_2 absorption lines and were subtracted from the spectra before the fitting of H_2 lines.

To analyze the spectra, we assigned the lines to *para* and *ortho* groups and confirmed this by measuring the spectrum of a *para* enriched H_2@C_{60} sample (Fig. 5). The 300 K spectra of the *para* enriched sample were measured at the day when sample arrived to Tallinn and again 19 days later [Fig. 5(b)]. The 20 K spectrum, measured on the day of arrival, is compared to the spectrum of a nonenriched sample. The 4255 cm^{-1} line is stronger and other three lines are weaker in the *para* enriched sample, as compared to the nonenriched sample. This proves that the previous assignment[6] of *ortho* and *para* lines in the 6 K spectrum was correct. The *ortho–para* ratio, $n_o/n_p = 2.890 \pm 0.045$, in the nonenriched sample was determined from the fit of the 6 K spectrum using the model Hamiltonian (Sec. II). Then this n_o/n_p and the areas of three lines, two *ortho* lines at 4250.7
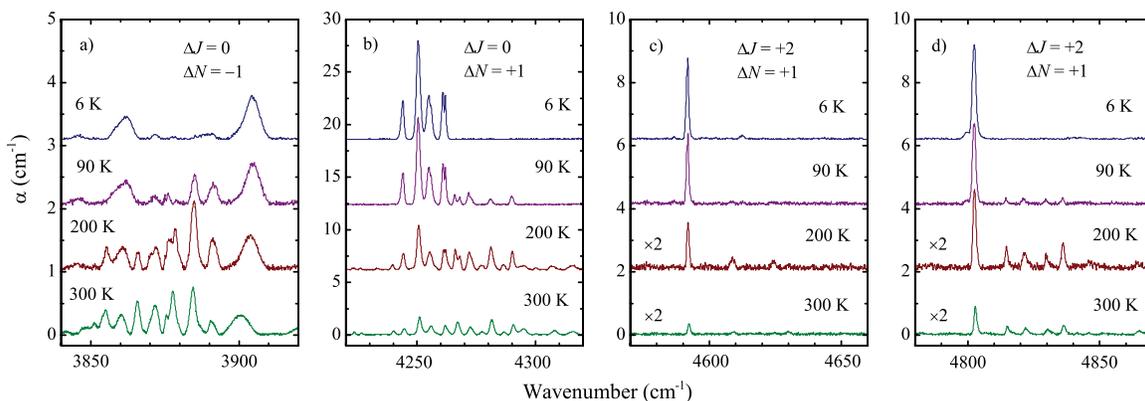

FIG. 4. Temperature dependence of the infrared absorption spectra of H_2@C_{60}. Four panels show groups of transitions with the same change of the quantum numbers J and N. An exception is the 4612.5 cm^{-1} line in (c), the fundamental *ortho*-H_2 transition $\Delta J = 2$, $\Delta N = 0$. Spectra are shifted vertically for clarification. Broad lines that are visible already in the 6 K spectrum below 4000 cm^{-1} in panel (a) are not H_2 absorption lines. The absorption of the 200 and 300 K spectra has been multiplied by 2 in panels (c) and (d).
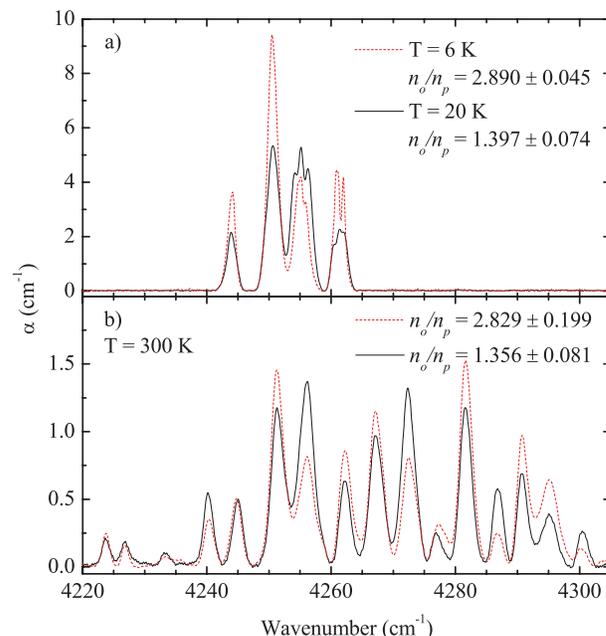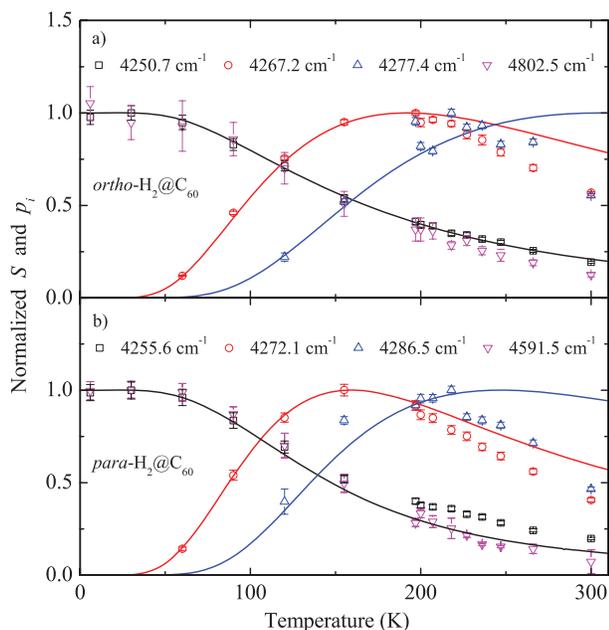
FIG. 6. Temperature dependence of selected IR absorption line areas S of *ortho*-H$_2$ (a) and *para*-H$_2$ (b) of transitions starting from states with $N = 0$ (squares and down triangles), $N = 1$ (circles) and $N = 2$ (up triangles). Solid lines are calculated [Eq. (21)] thermal population probabilities p_i of the corresponding initial states, as obtained from the model. S and p_i have been normalized to unity at their maxima. The error bars of S are from fitting the experimental lines with Gaussians.

and 4261 cm^{-1} and one *para* line at 4255 cm^{-1}, were used as calibration standards to calculate n_o/n_p for the *para* enriched sample. These lines were chosen because they are strong compared to other lines and at higher temperatures have the smallest overlap of *ortho* and *para* lines. We did not use the well-resolved low T *ortho* line at 4244 cm^{-1} because it overlaps with a *para* line at high T.

With increasing temperature the excited translational states, $N = 1$ and $N = 2$, become populated and the lines from $N = 0$ state become weaker. In Fig. 6 the normalized areas of several H$_2$@C$_{60}$ lines are compared to the temperature dependence of the normalized population probability of different initial states, $N = 0$, $N = 1$, and $N = 2$, using the eigenvalues obtained from fitting the 200 K spectrum with the model Hamiltonian. We see that within the error bars the temperature dependence of the normalized line areas is described very well up to 200 K. Above 200 K, there are deviations from the calculated curve, especially for lines starting from $N = 1$ and $N = 2$. These deviations could be due to the rotational motion of C$_{60}$ at higher temperatures. In solid C$_{60}$ there is a structural phase transition from the orientationally ordered low T phase to the high T phase where the molecules of C$_{60}$ rotate isotropically.[35–37] In H$_2$@C$_{60}$ the phase transition T is lowered from 260 to 240 K as the NMR study shows.[5]

The 200 K spectra were chosen for extensive study. This temperature was selected for the following reasons. *First*, at lower temperatures higher energy levels in the $v = 0$ state are insufficiently populated, and we lose information about the transitions involving these levels and terminal levels in the $v = 1$ state, reached by the selection rule $\Delta N = \pm 1$. This is essential in determining the harmonic and anharmonic terms

of the potential. *Second*, the 300 K spectrum does not add more information, as there are no new lines compared to the 200 K spectrum. We see from Fig. 4 and Table I that the change in positions of the H$_2$@C$_{60}$ lines is much less than the linewidth. Thus, the parameters determined at 200 K describe the system in the studied 6 to 300 K range relatively well.

Some of the lines in the 200 K spectrum or at lower T show small splittings. These are the lines at 4255, 4261, and 4267 cm^{-1} [Fig. 4(b)]. This splitting is not described by our model and could be due to the crystal field effects or inhomogeneities in the sample. In the synthetic spectrum, each of these three lines was treated as a single line. The fundamental lines with $\Delta v = 1$, $\Delta N = 0$, $\Delta J = 0$ were used in the fit to determine the fundamental frequency $\hbar\omega_0$. The fundamental *para* line (4071.4 cm^{-1}) is difficult to detect within the noise even below 60 K. However, the 4065.4 cm^{-1} *ortho* line can be tracked almost up to 200 K without showing any frequency shift. In the 6 K spectrum we see weak lines at 4587.0 and 4612.5 and a shoulder to the 4802.6 cm^{-1} line [Figs. 4(c) and 4(d)]. They originate from H$_2$@C$_{60}$, but are not described by the model Hamiltonian. The line at 4612.5 cm^{-1}, Table I, is probably the fundamental *ortho* transition with $\Delta J = 2$.

The best fit parameters at 200 K are listed in Table II. The *ortho–para* ratio, $n_o/n_p = 2.890 \pm 0.045$, was determined from the fit of the 6 K spectrum and was used here as a fixed parameter. A detailed result of fitting the absorption spectrum is shown in Fig. 7, where the experimental data are displayed in the form of a synthetic absorption spectrum together with the fit. The majority of absorption lines are reproduced by the model remarkably well with only some exceptions among the weaker lines, which are difficult to detect in the background noise. A spectral region around 4430 cm^{-1}, not present in Fig. 4, has been added and corresponds to $\Delta J = 2$, $\Delta N = -1$ *ortho* transitions [Fig. 7(c)]. The expected line at 4424 cm^{-1}, which is stronger than the 4407.4 cm^{-1} line, could not be resolved in the experimental spectrum due to a broad background absorption band between 4420 and 4430 cm^{-1}.

The experimental and fitted absorption lines are summarized in Table I, together with the dominant components of the initial and final eigenstates. Eigenstates are listed in Tables III and IV up to the highest states that are involved in the measured infrared transitions. For positive $^v V_{00}^{004}$, the distance between translational levels increases with the quantum number N. Also, the sign of $^v V_{00}^{004}$ determines the order of L levels for given N: the lowest energy level has the largest L. The ordering of Λ levels for given J, N, L is determined by the sign of $^v V_{00}^{222}$, which is positive in H$_2$@C$_{60}$ (Table II).

V. DISCUSSION

A. H$_2$ dynamics

The potential parameters $^v V_{00}^{ljn}$ are listed in Table II. The harmonic part of the potential $^v V_{00}^{002}$ gives, using Eq. (9), $^0\omega_0^T = 138.4$ cm^{-1} and $^1\omega_0^T = 146.1$ cm^{-1}. Thus, the anharmonic correction accounts for 22% of the energy difference of $N = 0$ and 1 levels, which are 179.5 and 184.4 cm^{-1} in the ground and excited vibrational states (Table III). The value

TABLE I. Experimental and calculated line positions, ω (cm^{-1}), and absorption line areas, S_ω (cm^{-2}), of IR-active modes at 200 K in H_2@C_{60}. The quantum numbers $JNL\Lambda$ and the relative weight $|\xi^v|^2$ of the main component contributing to the initial and final eigenstates are given. Experimental line positions and areas at 6 K are shown for comparison.

Experiment, 6 K		Experiment		Fitted		Initial state, $v=0$		Final state, $v=1$	
ω	S_ω	ω	S_ω	ω	S_ω	$JNL\Lambda$	$|\xi^0|^2$	$JNL\Lambda$	$|\xi^1|^2$
				para lines					
		3866.0	0.47	3866.0	0.09	0200	0.81	0111	0.94
		3872.2	1.18	3873.2	0.16	2113	0.91	2002	0.97
		3878.6	1.22	3878.4	0.35	0333	0.80	0222	0.89
		3884.9	2.80	3884.7	0.64	0222	0.85	0111	0.94
		3891.3	1.49	3891.8	0.77	0111	0.93	0000	0.98
4071.4	0.011			4071.3		0000	0.97	0000	0.98
		4223.3	0.28	4222.2	0.07	0111	0.93	2002	0.97
		4233.1	0.22	4233.1	0.22	2002	0.95	2112	0.95
		4239.8	0.64	4239.6	0.64	2002	0.95	2113	0.93
		4244.4	2.54	4244.5	0.47	2002	0.95	2111	0.94
		4250.7	7.83	4252.5	0.20	2112	0.94	2223	0.90
4255.2	10.60	4255.6	4.29	4255.8	3.65	0000	0.97	0111	0.94
		4261.3	4.11	4261.8	0.08	2111	0.92	2220	0.89
		4272.1	3.70	4272.1	2.78	0111	0.93	0222	0.89
		4286.5	0.89	4286.4	1.41	0222	0.85	0333	0.83
		4290.2	2.72	4289.9	0.49	0111	0.93	0200	0.84
		4294.8	1.08	4294.8	0.28	0200	0.81	0311	0.72
4592.0	3.08	4592.0	0.90	4592.4	0.79	0000	0.97	2111	0.94
		4608.9	0.37	4608.9	0.31	0111	0.93	2221	0.89
		4624.3	0.27	4624.5	0.25	0111	0.93	2202	0.74
		4630.0	0.10	4629.4	0.12	0222	0.85	2331	0.82
				ortho lines					
		3855.6	0.77	3855.6	0.41	1201	0.62	1112	0.94
		3866.0	0.47	3866.1	0.27	1201	0.62	1110	0.94
		3872.2	1.18	3871.6	0.38	1221	0.68	1111	0.95
				3872.4	0.71	1334	0.81	1223	0.89
		3876.0	1.13	3874.9	0.27	1333	0.83	1222	0.90
				3876.3	0.85	1110	0.92	1001	0.98
		3878.6	1.22	3878.5	1.25	1223	0.88	1112	0.94
		3884.9	2.80	3884.9	1.88	1112	0.93	1001	0.98
		3891.3	1.49	3890.5	0.50	1111	0.94	1001	0.98
4065.4	0.093			4065.4		1001	0.97	1001	0.98
		4223.3	0.28	4222.7	0.24	3003	0.97	3114	0.94
		4226.2	0.21	4225.3	0.17	3003	0.97	3112	0.94
4244.5	5.76	4244.4	2.54	4244.4	1.95	1001	0.97	1111	0.95
		4250.7	7.83	4250.9	7.71	1001	0.97	1112	0.94
		4255.6	4.29	4257.3	0.22	1112	0.93	1222	0.90
4261.0	8.86	4261.3	4.11	4261.4	3.74	1001	0.97	1110	0.94
				4262.8	2.10	1111	0.94	1222	0.90
		4267.1	4.26	4267.0	5.48	1112	0.93	1223	0.89
		4272.1	3.70	4272.7	1.77	1111	0.94	1221	0.65
		4277.1	0.82	4277.2	1.27	1222	0.89	1333	0.85
		4281.2	4.33	4281.2	4.90	1223	0.88	1334	0.84
		4290.2	2.72	4289.7	2.13	1112	0.93	1201	0.61
				4291.3	0.90	1201	0.62	1312	0.59
		4294.8	1.08	4296.2	0.26	1221	0.68	1311	0.74
		4300.0	0.30	4298.3	0.001	1334	0.81	1444	0.86
		4306.7	0.92	4305.2	0.19	1222	0.89	1311	0.74
		4316.4	1.37	4316.8	0.84	1334	0.81	1445	0.85
				4318.4	0.51	1332	0.68	1443	0.77
		4407.4	0.05	4407.2	0.07	1201	0.62	3112	0.94
		4426.8	0.35	4427.4	0.34	1223	0.88	3114	0.94
				4428.0	0.06	1222	0.89	3113	0.95
		4431.9	0.44	4432.5	0.53	1112	0.93	3003	0.98
4612.5	0.30			4613.1		1001	0.97	3003	0.97

TABLE I. (*Continued*)

Experiment, 6 K		Experiment		Fitted		Initial state, $v = 0$		Final state, $v = 1$	
ω	S_ω	ω	S_ω	ω	S_ω	$JNL\Lambda$	$\|\xi^0\|^2$	$JNL\Lambda$	$\|\xi^1\|^2$
4802.5	5.65	4802.6	1.80	4802.5	1.94	1001	0.97	3112	0.94
		4814.8	0.39	4815.5	0.16	1112	0.93	3222	0.89
				4816.2	0.32	1110	0.92	3221	0.75
		4821.6	0.49	4821.0	0.52	1111	0.94	3222	0.89
		4829.7	0.26	4830.3	0.30	1111	0.94	3221	0.75
		4836.2	0.55	4835.8	0.66	1112	0.93	3203	0.72
		4846.4	0.23	4845.2	0.05	1222	0.89	3331	0.81
				4848.1	0.03	1223	0.88	3313	0.62
		4864.5	0.17	4862.9	0.02	1221	0.68	3312	0.67
				4864.8	0.03	1333	0.83	3444	0.81

179.5 cm^{-1} of the separation of the first two translational levels in the $v = 0$ state is consistent with the result of the INS experiment,[8] where it is 179.9 cm^{-1}.

The harmonic part $^vV_{00}^{002}$ is larger in the excited $v = 1$ state than in the ground state, while the anharmonic part $^vV_{00}^{004}$ is slightly larger in the ground state. The same trend holds for the harmonic and anharmonic parts of the translation–rotation coupling potential parameters, although there the differences between the potential parameters in $v = 0$ and 1 states are even bigger. The translation–rotation coupling $^1V_{00}^{222}$ in the excited state is two times bigger than $^0V_{00}^{222}$ in the ground state. This difference is partially eliminated by the reversed magnitudes of anharmonic potential parameters as $^1V_{00}^{224}$ is about two times smaller than $^0V_{00}^{224}$. The separation of energy levels in the $J = N = 1$ states is $E_{1110}^0 - E_{1111}^0 = 14.2$ cm^{-1} and $E_{1110}^1 - E_{1111}^1 = 17.0$ cm^{-1} (Table IV). Thus, the translation–rotation splitting remains larger for the $v = 1$ state but not as much as if anharmonic terms $^vV_{00}^{224}$ were zero.

The translation–rotation splitting is the distance between levels with different Λ but same J, N, and L. Closer inspection of Tables III and IV shows that starting from $E_{J31\Lambda}^v$ for all $N > 3$ the translation–rotation splitting is larger in the $v = 0$ state than in the $v = 1$ state. This is because $^0V_{00}^{224} > {}^1V_{00}^{224}$. The result that the strength of the translation–rotation coupling in two different vibrational states shows crossover at $N = 3$ is based on the current interpretation of IR spectra where the largest N value represented in the ground state is $N = 2$ and thus has no direct experimental proof.

TABLE II. Values of the fitted parameters κ_i.

κ_i	$v = 0$	$v = 1$	Unit
$^vV_{00}^{002}$	14.277 ± 0.034	15.952 ± 0.032	Jm^{-2}
$^vV_{00}^{222}$	0.5629 ± 0.0059	1.199 ± 0.012	Jm^{-2}
$^vV_{00}^{004}$	$(2.2105 \pm 0.0099)10^{21}$	$(2.1920 \pm 0.0085)10^{21}$	Jm^{-4}
$^vV_{00}^{224}$	$(2.211 \pm 0.023)10^{20}$	$(1.030 \pm 0.011)10^{20}$	Jm^{-4}
$\hbar\omega_0$	4062.37 ± 0.28		cm^{-1}
B_e	59.865 ± 0.074		cm^{-1}
α_e	2.974 ± 0.025		cm^{-1}
D_e	$(4.832 \pm 0.051)10^{-2}$		cm^{-1}
$B_{10}[10]$	$(4.53 \pm 0.13)10^{-23}$		C
$B_{10}[12]$	$(-2.13 \pm 0.21)10^{-23}$		C
n_o/n_p	2.890 ± 0.045		

We reported[6] that the vibrational frequency ω_0 is equal to the frequency of the fundamental *para* transition at $\omega = 4071.4$ cm^{-1}. This is true if the zero-point translational energies are equal in $v = 0$ and 1 states. Now when we have determined the ground state potential as well, we see that the vibrational frequency is $\omega_0 = 4062.4$ cm^{-1}. The difference of the observed fundamental *para* line frequency $\omega = 4071.4$ cm^{-1} from the vibrational frequency ω_0 is determined by the different zero-point

TABLE III. Calculated energy levels of *para*-H$_2$ inside C$_{60}$ for the ground and excited states up to $JNL\Lambda = 2311$. The excitation energies ΔE_{para}^0 and ΔE_{para}^1 (in cm^{-1}) are relative to the ground state energy $E_{0000}^0 = 2274.07$ cm^{-1} and $E_{0000}^1 = 6345.39$ cm^{-1}. $\|\xi\|^2$ is the contribution of the dominant quantum basis $|JNL\Lambda\rangle$ to the particular eigenstate.

| Initial state, $v = 0$			Final state, $v = 1$		
$JNL\Lambda$	ΔE_{para}^0	$\|\xi^0\|^2$	$JNL\Lambda$	ΔE_{para}^1	$\|\xi^1\|^2$
0000	0.0	0.97	0000	0.0	0.98
0111	179.5	0.93	0111	184.4	0.94
2002	347.9	0.95	2002	330.3	0.97
0222	371.1	0.85	0222	380.3	0.89
0200	389.7	0.81	0200	398.1	0.84
2112	523.5	0.94	2112	509.7	0.95
2113	528.5	0.91	2113	516.2	0.93
2111	532.7	0.92	2111	521.1	0.94
0333	573.2	0.80	0333	586.2	0.83
0311	601.9	0.68	0311	613.2	0.72
2223	713.6	0.88	2223	704.6	0.90
2222	714.7	0.80	2222	705.8	0.80
2224	721.2	0.87	2224	713.3	0.89
2221	724.8	0.87	2221	717.0	0.89
2220	730.0	0.87	2220	723.2	0.89
2202	741.5	0.72	2202	732.6	0.74
0444	815.3	0.84	0444	823.2	0.85
0422	878.1	0.67	0422	877.4	0.70
0400	906.4	0.61	0400	901.8	0.65
2333	914.1	0.78	2334	909.4	0.85
2334	914.4	0.82	2333	909.4	0.80
2332	921.6	0.71	2332	917.1	0.72
2335	924.7	0.81	2335	920.4	0.83
2331	933.3	0.80	2331	929.2	0.82
2312	943.9	0.60	2312	937.8	0.62
2313	956.7	0.63	2313	950.3	0.67
2311	963.1	0.66	2311	956.5	0.70
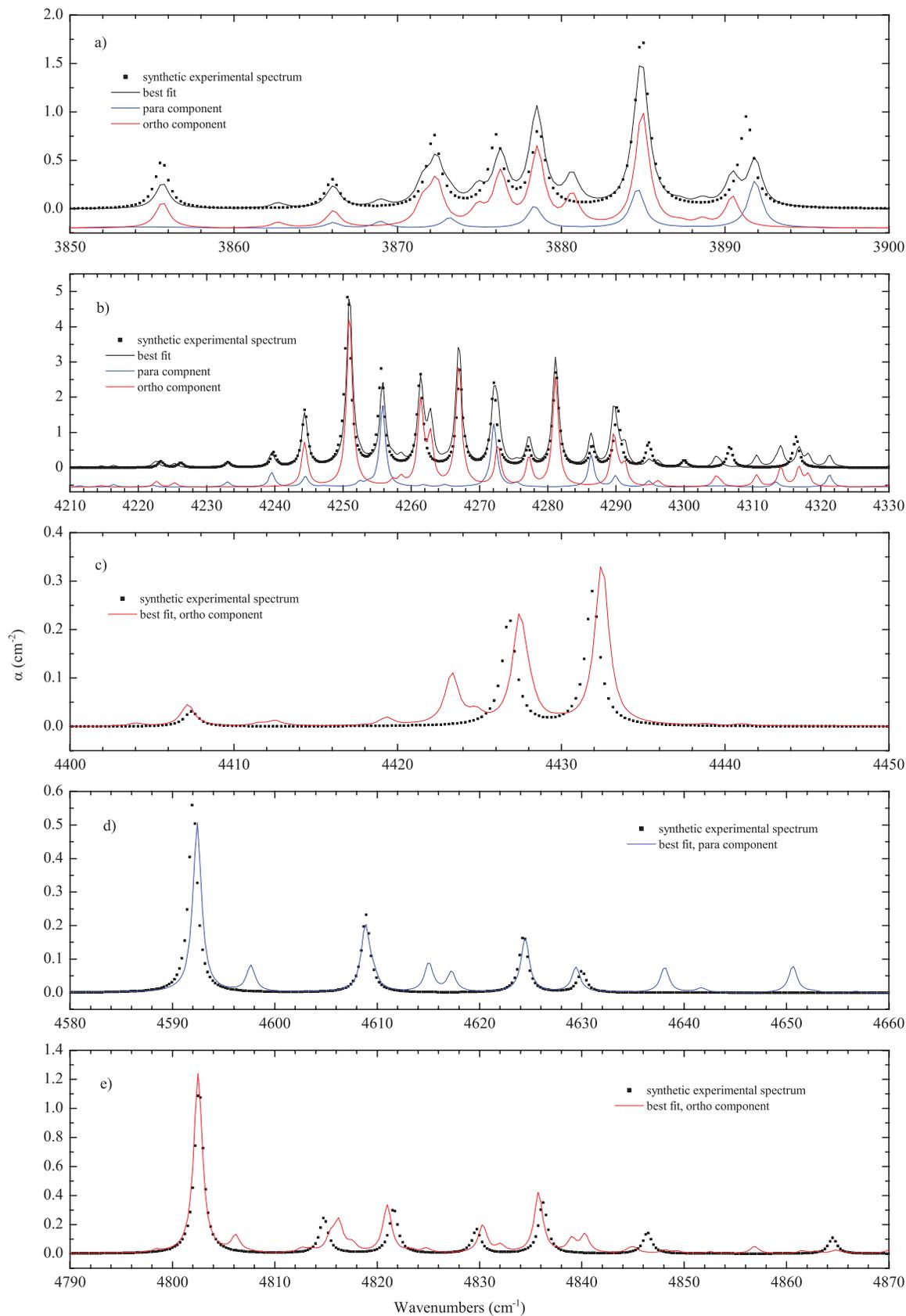
FIG. 7. Synthetic experimental absorption spectra of $H_2@C_{60}$ at 200 K (dots) together with the fit result, FWHM $= 1$ cm^{-1}. The total absorbance α is the sum of *para* and *ortho* components, shifted in vertical direction for clarity and shown separately in panels (a) and (b), where both components have a significant contribution. Above 4400 cm^{-1} only *para*, panel (d), or *ortho*, panels (c) and (e), components of the fit are shown, as the other component does not have any contribution.

TABLE IV. Calculated energy levels of *ortho*-H$_2$ inside C$_{60}$ for the ground and excited states up to $JNL\Lambda = 3444$. The excitation energies ΔE^0_{ortho} and ΔE^1_{ortho} (in cm^{-1}) are relative to the ground state energy E^0_{1001} = 2390.61 cm^{-1} and E^1_{1001} = 6455.98 cm^{-1}. $|\xi|^2$ is the contribution of the dominant quantum basis $|JNL\Lambda\rangle$ to the particular eigenstate.

Initial state, $v = 0$			Final state, $v = 1$		
$JNL\Lambda$	ΔE^0_{para}	$|\xi^0|^2$	$JNL\Lambda$	ΔE^1_{para}	$|\xi^1|^2$
1001	0.0	0.97	1001	0.0	0.98
1111	174.9	0.94	1111	179.0	0.95
1112	180.4	0.93	1112	185.6	0.94
1110	189.1	0.92	1110	196.0	0.94
1222	363.7	0.89	1222	372.4	0.90
1223	372.4	0.88	1223	382.0	0.89
1221	372.8	0.68	1221	382.2	0.65
1201	395.3	0.62	1201	404.7	0.61
1333	562.8	0.83	3003	547.5	0.98
1332	575.0	0.68	1333	575.6	0.85
1334	575.1	0.81	1334	588.3	0.84
3003	577.2	0.97	1332	588.6	0.69
1311	591.9	0.70	1311	603.6	0.74
1312	609.8	0.56	1312	621.2	0.59
1310	623.6	0.65	1310	634.6	0.70
3113	752.0	0.94	3113	726.4	0.95
3114	758.7	0.93	3114	734.5	0.94
3112	761.0	0.93	3112	737.1	0.94
1444	799.0	0.85	1444	808.1	0.86
1445	819.6	0.84	1445	826.6	0.85
1443	819.7	0.76	1443	827.8	0.77
1422	860.2	0.69	1422	862.1	0.72
1421	875.9	0.39	1421	876.0	0.41
1423	892.8	0.58	1423	888.8	0.61
1401	933.1	0.31	3223	921.2	0.79
3223	942.1	0.79	1401	922.2	0.31
3224	943.0	0.88	3224	922.2	0.90
3222	950.5	0.87	3222	930.5	0.89
3225	952.5	0.86	3225	933.0	0.88
3221	958.9	0.78	3221	940.0	0.75
3203	971.5	0.71	3203	950.8	0.72
1555	1038.2	0.83	1555	1046.0	0.84
1556	1064.6	0.80	1556	1068.1	0.80
1554	1066.3	0.75	1554	1071.6	0.77
1533	1127.9	0.57	1533	1123.0	0.48
3334	1141.0	0.79	3334	1124.6	0.81
3335	1144.9	0.82	3335	1128.3	0.84
3333	1146.1	0.67	3333	1130.4	0.52
3332	1152.2	0.29	3332	1137.4	0.81
3332	1154.8	0.51	3336	1142.8	0.79
3336	1158.4	0.78	3331	1143.5	0.81
3331	1158.7	0.76	1532	1146.3	0.43
3330	1163.4	0.81	3330	1147.7	0.83
1534	1166.3	0.35	1534	1151.7	0.34
3313	1173.2	0.59	3313	1155.2	0.62
1511	1185.1	0.47	3312	1170.3	0.67
3312	1188.6	0.63	1511	1173.4	0.53
3314	1195.9	0.40	3314	1177.8	0.39
1512	1248.7	0.33	1512	1221.6	0.38
1510	1277.5	0.47	1510	1244.5	0.51
3445	1379.7	0.83	3445	1359.1	0.84
3444	1383.0	0.80	3444	1362.3	0.81

translational energies in $v = 0$ and 1 states. In the harmonic approximation the difference is $\frac{3}{2}(^1\omega^T_0 - {}^0\omega^T_0) = 11.6$ cm^{-1}, but is reduced to 9.0 cm^{-1} because of anharmonic corrections $^vV^{004}_{00}$. The vibrational frequency ω_0 is redshifted by 98.8 cm^{-1} from its gas phase value,[38] 4161.2 cm^{-1}. At this point we cannot say how much of this redshift is caused by change in the zero-point vibrational energy and how much is caused by the change of anharmonic corrections to the vibrational levels in the C$_{60}$ as our data set is limited to energy differences of $v = 0$ and 1 levels only.

The rotational constant B_e and the vibrational correction α_e of H$_2$ inside C$_{60}$, Table II, are smaller than the gas phase values,[38] 60.853 and 3.062 cm^{-1}. We found that it is necessary to include a centrifugal correction D_e to the rotational constant, that is quite close to the gas phase value of 0.0471 cm^{-1}.[38] Without this correction it is not possible to fit the frequencies of S(0) and S(1) lines, as is seen in Fig. 1 of Ref. 6. The value of B_e smaller than the gas phase value may be interpreted as 0.81% stretching of the proton–proton distance s in H$_2$@C$_{60}$, as $B_e \sim \langle 1/s^2 \rangle$. An attractive interaction between hydrogen atoms and the cage causes s to be longer. The elongation of the equilibrium proton-proton distance is consistent with the redshift of ω_0 (Ref. 39). However, the correction α_e is smaller inside the cage than in the gas phase. Here the cage has the opposite, repulsive, effect and reduces the elongation of the proton-proton distance in the excited v states when compared to H$_2$ being in the free space. The repulsive effect of the cage follows from the *positive* anharmonic corrections to the translational levels as well.

Xu *et al.*[11] introduced a three site Lennard-Jones potential to reproduce the translation–rotation levels observed in low T IR spectra. They found the best set of potential parameters for the $N = 0$ and 1 levels in the $v = 1$ state, which reproduced the observed IR frequencies very well, within 0.6%. Comparison with additional data available now shows that differences become bigger as N increases, and the trend is the same for *para* $J = 0$ and *ortho* $J = 1$ states. When compared to energies listed in Tables III and IV, their energies $E^1_{J20\Lambda}$ and $E^1_{J33\Lambda}$ are higher by 10 cm^{-1} and $E^1_{J31\Lambda}$ by 25 cm^{-1}. Xu *et al.* found that three different parameter sets fitted the 6 K data equally well. Since higher T data were not available at the time, it was not possible to judge which parameter set is the best to reproduce the anharmonic part of the potential.

The symmetry of C$_{60}$ is icosahedral. Within this symmetry the degeneracy of a $\Lambda = 3$ level is lifted. The possible candidate to study the $\Lambda = 3$ level splitting in the IR spectrum is the *ortho* line at 4267 cm^{-1} (Table I). This experimental line is split into two components, about 2 cm^{-1} apart [see 90 and 200 K spectra in Fig. 4(b)]. According to our fit with the spherically symmetric potential, it is the $|1112\rangle \rightarrow |1223\rangle$ transition and has no other *ortho* or *para* lines within 2 cm^{-1} [Fig. 7(b)]. However, it is unlikely that the splitting of the 4267 cm^{-1} line is caused by the icosahedral symmetry because the calculation of Xu *et al.*[11] shows that the splitting of this $\Lambda = 3$ level should be only 0.5 cm^{-1}.

A similar system to the one studied here is exohedral H$_2$ in C$_{60}$. There H$_2$ occupies the octahedral interstitial site

in the C_{60} crystal. The prominent features in the exohedral H_2 IR spectra[40] are the translational, $\Delta N = \pm 1$, sidebands to the fundamental transitions, $\Delta v = 1$ and $\Delta J = 0, 2$. The redshift of the fundamental vibrational frequency is about 60 cm^{-1}, which is less than that in $H_2@C_{60}$ where it is 98.8 cm^{-1}. Also the separation of translational $N = 0$ and 1 levels, approximately 120 cm^{-1}, is smaller, when compared to 184.4 cm^{-1} in $H_2@C_{60}$. It is likely that the main contribution to the latter difference comes from the larger van der Waals volume available for H_2 in the octahedral site than in the C_{60} cage.

B. Dipole moment

The dipole moment parameters $B_{10}[10]$ and $B_{10}[12]$ are given in Table II. The numerical values are consistent with our previous result,[6] where only the ratio of the two dipole moment parameters, -2.0 ± 0.2, was given. The choice of which is negative is arbitrary as the line intensities are insensitive to the sign change of the two parameters. The listed $B_{10}[lj]$ depend on the pairwise H_2–C induced dipole parameter B^{lj} and its derivative [Eq. (14)]. A theoretical calculation of B^{lj} for H_2–C is outside the scope of the current study. The general trend is consistent with the theoretical calculations for H_2–He pairs, where the signs of B^{10} and B^{12} are opposite and B^{12} has the smaller absolute value.[25]

Herman and Lewis[41] calculated the dipole moment of interstitial H_2 at the octahedral site in solid C_{60} using H_2–He interaction data. They considered the isotropic exchange (overlap) induced dipole (B^{10}) at short range and the quadrupole induced dipole (B^{32}) at short and long ranges. We showed in Sec. II that B^{32} does not contribute to $\Delta N = \pm 1$ electric dipole transitions in endohedral H_2.

The dipole moment calculated from the 6 K area $S = 10.6$ cm^{-2} of the 4255 cm^{-1} *ortho* line (Table I) using Eq. (20) gives $d = 3.28 \times 10^{-32}$ Cm $= 9.83 \times 10^{-3}$ D. For example, the permanent dipole moment of a free HD molecule[42] corresponding to $v = 0 \rightarrow 1$, $J \rightarrow J + 1$ transitions is only 5×10^{-5} D. To estimate an effective charge associated with the 4255 cm^{-1} transition, we use $q = 20 B_{10}[10]$ [see Eq. (13)] and get $q = 9.1 \times 10^{-22}$ C after substituting the fitted value for $B_{10}[10]$ from Table II. This is about 0.006 electron charges. However, the displacement $\langle R \rangle_{10} = d/q = 0.36$ Å associated with this dipole moment is comparable to the typical atomic scale, the Bohr radius. Thus, the small dipole moment is mainly the consequence of the small induced charge disproportionation of the $H_2@C_{60}$, when H_2 experiences translational motion in the C_{60} cage.

The IR transitions reported here are the transitions where the vibrational state changes, $v = 0 \rightarrow 1$. One may ask if the induced electric dipole transitions, $\Delta N = \pm 1$, can be observed within the vibrational ground state $v = 0$. The difference between these two kinds of transitions lies in the dependence of the dipole moment on the proton–proton distance s, represented by the parameter $A_{v'v}^{lj}(R)$ [Eq. (13)]. The expectation value of R is very similar for both transitions and does not account for the observed difference as explained below. We did not see the transitions of H_2 in far-IR, but can set the upper limit to the dipole moment. The experiment was conducted on a 1.9 mm thick pellet at 20 K. The strongest line expected is the overlap of a *para* line at 179.5 cm^{-1} ($|0000\rangle \rightarrow |0111\rangle$) and *ortho* line at 180.4 cm^{-1} ($|1001\rangle \rightarrow |1112\rangle$) (Tables III and IV). The intensity of both lines is given by A_{00}^{10}. We simulated the expected absorption using Eq. (17) (note the dependence on ω) and saw that it is at least ten times stronger than would have been possible to detect within our noise level. Thus, in the ground vibrational state, the induced dipole moment must be suppressed at least by a factor of $A_{10}^{10}/A_{00}^{10} \geq \sqrt{10}$. It has been found that the induced dipole moments of a H_2–He pair have an opposite dependence on the vibrational states,[25] B_{00}^{10} is larger than B_{10}^{10}.

VI. SUMMARY

The IR absorption spectrum of endohedral H_2 in C_{60} is rich, involving several excitations: vibrations, rotations, and translational motions of H_2. The translational motion is quantized because of the surrounding C_{60} cage and coupled to the rotations of H_2. We used a model of a vibrating rotor in a spherical potential together with the translational motion induced dipole moment theory to explain the positions and intensities of IR absorption lines (Table I). The main effect of temperature on the IR spectra in the studied range 6–300 K is the change of IR line intensities, which is reasonably well accounted for by the Boltzmann distribution in the ground vibrational state $v = 0$. The energy levels of $H_2@C_{60}$ are given in Tables III and IV and were calculated from the model using parameters given in Table II. The potential parameters show clear dependence on the vibrational state, $v = 0$ or $v = 1$. The potential is divided into an isotropic part, which depends on the center of mass coordinate of H_2 and an anisotropic part which depends on the orientation of H_2 molecule. The IR spectra can be fitted only if both parts of the potential are anharmonic. The induced dipole moment must depend on the vibrational coordinate as well, otherwise we cannot explain why we did not observe far-IR $\Delta N = 1$ transitions in the ground vibrational state $v = 0$.

Our study shows that the vibrations and rotations of C_{60} and the crystal field effects of solid C_{60} are not important on the energy scale of IR measurements. If these effects are important, their contribution to the IR spectra is the order of 1 wavenumber splitting of few absorption lines. Such small splitting is consistent with the results of heat capacity measurements.[43]

We do not explain how the determined parameters are linked to the molecular structure of the $H_2@C_{60}$ complex. In principle it should be possible to describe, within a single quantum chemical model of $H_2@C_{60}$, the potential parameters, induced dipole parameters, the dependence of both on the vibrational state, and the changes of rotational and vibrational constants compared to free H_2 values. Some additional information may come from the IR studies of endohedral D_2 and HD, a work in progress.

ACKNOWLEDGMENTS

[1]Y. Rubin, T. Jarrosson, G.-W. Wang, M. D. Bartberger, K. N. Houk, G. Schick, M. Saunders, and R. J. Cross, Angew. Chem., Int. Ed. **40**, 1543 (2001).

[2]K. Komatsu, M. Murata, and Y. Murata, Science **307**, 238 (2005).

[3]M. Murata, Y. Murata, and K. Komatsu, J. Am. Chem. Soc. **128**, 8024 (2006).

[4]M. Carravetta, O. G. Johannessen, M. H. Levitt, I. Heinmaa, R. Stern, A. Samoson, A. J. Horsewill, Y. Murata, and K. Komatsu, J. Chem. Phys. **124**, 104507 (2006).

[5]M. Carravetta, A. Danquigny, S. Mamone, F. Cuda, O. G. Johannessen, I. Heinmaa, K. Panesar, R. Stern, M. C. Grossel, A. J. Horsewill, A. Samoson, M. Murata, Y. Murata, K. Komatsu, and M. H. Levitt, Phys. Chem. Chem. Phys. **9**, 4879 (2007).

[6]S. Mamone, M. Ge, D. Hüvonen, U. Nagel, A. Danquigny, F. Cuda, M. C. Grossel, Y. Murata, K. Komatsu, M. H. Levitt, T. Rõõm, and M. Carravetta, J. Chem. Phys. **130**, (2009).

[7]A. J. Horsewill, K. S. Panesar, S. Rols, M. R. Johnson, Y. Murata, K. Komatsu, S. Mamone, A. Danquigny, F. Cuda, S. Maltsev, M. C. Grossel, M. Carravetta, and M. H. Levitt, Phys. Rev. Lett. **102**, 013001 (2009).

[8]A. J. Horsewill, S. Rols, M. R. Johnson, Y. Murata, M. Murata, K. Komatsu, M. Carravetta, S. Mamone, M. H. Levitt, J. Y.-C. Chen, J. A. Johnson, X. Lei, and N. J. Turro, Phys. Rev. B **82**, 081410 (2010).

[9]M. Xu, F. Sebastianelli, Z. Bačić, R. Lawler, and N. J. Turro, J. Chem. Phys. **128**, 011101 (2008).

[10]M. Xu, F. Sebastianelli, Z. Bačić, R. Lawler, and N. J. Turro, J. Chem. Phys. **129**, 064313 (2008).

[11]M. Xu, F. Sebastianelli, B. R. Gibbons, Z. Bačić, R. Lawler, and N. J. Turro, J. Chem. Phys. **130**, 224306 (2009).

[12]F. Sebastianelli, M. Xu, Z. Bačić, R. Lawler, and N. J. Turro, J. Am. Chem. Soc. **132**, 9826 (2010).

[13]S. Mamone, J. Y.-C. M. Chen, R. Bhattacharyya, M. H. Levitt, R. G. Lawler, A. J. Anthony J Horsewill, T. Rõõm, Z. Bačić, and N. J. Turro, "Theory and spectroscopy of an incarcerated quantum rotor: The infrared spectroscopy, inelastic neutron ccattering and nuclear magnetic resonance of H$_2$C$_{60}$ at cryogenic temperature," Coord. Chem. Rev. (2011).

[14]E. H. T. Olthof, A. van der Avoird, and P. E. S. Wormer, J. Chem. Phys. **104**, 832 (1996).

[15]M. Krause, M. Hulman, H. Kuzmany, O. Dubay, G. Kresse, K. Vietze, G. Seifert, C. Wang, and H. Shinohara, Phys. Rev. Lett. **93**, 137403 (2004).

[16]K. H. Michel, B. Verberck, M. Hulman, H. Kuzmany, and M. Krause, J. Chem. Phys. **126**, 064304 (2007).

[17]R. J. Cross, J. Phys. Chem. A **105**, 6943 (2001).

[18]T. Yildirim and A. B. Harris, Phys. Rev. B **66**, 214301 (2002).

[19]N. J. Turro, A. A. Marti, J. Y.-C. Chen, S. Jockusch, R. G. Lawler, M. Ruzzi, E. Sartori, S.-C. Chuang, K. Komatsu, and Y. Murata, J. Am. Chem. Soc. **130**, 10506 (2008).

[20]N. J. Turro, J. Y.-C. Chen, M. Sartori, E. Ruzzi, A. A. Marti, R. G. Lawler, S. Jockusch, J. López-Gejo, K. Komatsu, and Y. Murata, Acc. Chem. Res. **43**, 335 (2010).

[21]S. Flügge, *Practical Quantum Mechanics* (Springer-Verlag, Berlin, 1971).

[22]D. A. Varshalovich, A. N. Moskalev, and V. K. Kheronskii, *Quantum Theory of Angular Momentum* (World Scientific, Singapore, 1988).

[23]G. Herzberg, *Molecular Spectra and Molecular Structure, I. Spectra of Diatomic Molecules*, 2nd ed. (Van Nostrand, Princeton, 1950).

[24]J. L. Dunham, Phys. Rev. **41**, 721 (1932).

[25]L. Frommhold, *Collisison-Induced Absorption in Gases*, Cambridge Monographs on Atomic, Molecular, and Chemical Physics, Vol. 2 (Cambridge University Press, Cambridge, England, 1993).

[26]R. M. Berns, P. E. S. Wormer, F. Mulder, and A. van der Avoird, J. Chem. Phys. **69**, 2102 (1978).

[27]P. E. S. Wormer and G. V. Dijk, J. Chem. Phys. **70**, 5695 (1979).

[28]W. Meyer and L. Frommhold, Phys. Rev. A **34**, 2771 (1986).

[29]L. Frommhold and W. Meyer, Phys. Rev. A **35**, 632 (1987).

[30]M. Gustafsson, L. Frommhold, and W. Meyer, J. Chem. Phys. **113**, 3641 (2000).

[31]J. D. Poll and J. L. Hunt, Can. J. Phys. **54**, 461 (1976).

[32]C. C. Homes, P. J. Horoyski, M. L.W. Thewalt, and B. P. Clayman, Phys. Rev. B **49**, 7052 (1994).

[33]W. Gordy and R. L. Cook, *Microwave Molecular Spectra*, 3rd ed., Techniques of Chemistry, Vol. 18 (Wiley-Interscience, New York, 1984).

[34]M. C. Martin, X. Du, J. Kwon, and L. Mihaly, Phys. Rev. B **50**, 173 (1994).

[35]P. A. Heiney, J. E. Fischer, A. R. McGhie, W. J. Romanow, A. M. Denenstein, J. P. McCauley, Jr., A. B. Smith, and D. E. Cox, Phys. Rev. Lett. **66**, 2911 (1991).

[36]R. Tycko, G. Dabbagh, R. M. Fleming, R. C. Haddon, A. V. Makhija, and S. M. Zahurak, Phys. Rev. Lett. **67**, 1886 (1991).

[37]W. I. F. David, R. M. Ibberson, T. J. S. Dennis, J. P. Hare, and K. Prassides, Europhys. Lett. **18**, 219 (1992).

[38]K. P. Huber and G. Herzberg, *Constants of Diatomic Molecules*, Molecular Spectra and Molecular Structure, Vol. IV (Van Nostrand, New York, 1979).

[39]C. G. Van de Walle, Phys. Rev. Lett. **80**, 2177 (1998).

[40]S. A. FitzGerald, H. O. H. Churchill, P. M. Korngut, C. B. Simmons, and Y. E. Strangas, Phys. Rev. B **73**, 155409 (2006).

[41]R. M. Herman and J. C. Lewis, Phys. Rev. B **73**, 155408 (2006).

[42]K. Pachucki and J. Komasa, Phys. Rev. A **78**, 052503 (2008).

[43]Y. Kohama, T. Rachi, J. Jing, Z. Li, J. Tang, R. Kumashiro, S. Izumisawa, H. Kawaji, T. Atake, H. Sawa, Y. Murata, K. Komatsu, and K. Tanigaki, Phys. Rev. Lett. **103**, 073001 (2009).